A Novel Range Processing Method of Surface-Based FMCW Ice-Sounding Radar for Accurately Mapping the Internal Reflecting Horizons in Antarctica

Shinan Lang, *Member, IEEE*, Xiangbin Cui, Yukai Zhao, Ben Xu, Xiaojun Liu, Yiheng Cai, *Member, IEEE*, and Qiang Wu

***Abstract*—In this article, we establish the nonlinear signal model of the surface-based frequency-modulated continuous wave ice-sounding radar, and propose a novel range processing strategy that aims at removing the frequency ramp nonlinearity effectively. The proposed algorithm takes full consideration of the dependence of nonlinearity on the round-trip delay time while providing certain robustness of noise. The theory analysis and implementation steps of the proposed algorithm are demonstrated. The full-scale simulations with different kinds of nonlinearities and various signal-to-noise ratios verify the effectiveness and robustness of the proposed algorithm. We also apply the proposed method to real dataset collected during the 31st Chinese Antarctic Research Expedition (CHINARE 31) and CHINARE 33. The result shows the effectiveness of our algorithm on illustrating clarified internal reflecting horizons of ice sheets. Compared with the echograms processed by the typical range processing scheme, our algorithm performs better in nonlinearity elimination.**

***Index Terms*—Frequency-modulated continuous wave (FMCW) ice-sounding radar, frequency ramp nonlinearity, nonlinear signal model, signal-to-noise ratio (SNR).**

I. Introduction

In CONTRARY to the conventional ice-sounding radar works in pulsed mode [1]–[3], the frequency-modulated continuous wave (FMCW) radar requires less peak transmit power and offers the benefits of compacted size, light weight, low power cost, and high range resolution [4]. According to aforementioned features, the FMCW radar has been used extensively for the airborne and surface-based measurements of air-snow and snow-ice interfaces to evaluate the snow thickness on top of the sea ice, and mapping of internal reflecting horizons (IRHs) within polar firn to determine the annual snow/firn accumulation on glaciers and ice sheets [5].

The surface-based FMCW ice-sounding radar's ability to clearly map the aforementioned interfaces depends on highly accurate signal processing in two dimensions, i.e., range and along-track direction. In the along-track direction, the surface conditions are taken into consideration when the rough surfaces arise [5]. The unfocused synthetic aperture radar (SAR) is applied to reduce the size of along-track footprint to some extent [11] in order to promote the radar's ability to accurately map the interfaces in the along-track direction. There are lots of related works that focus on the unfocused SAR algorithm applied to the FMCW ice-sounding radar [5], [7], [10]. Hence, we skip the signal processing in the along-track direction in this article. To achieve the unambiguously high-precision range profile, the clear and comprehensive signal processing technique in the range direction should be presented. Brennan *et al.* [22], Li *et al.* [13], Yan *et al.* [5], [6], and Panzer *et al.* [7] proposed several typical range processing schemes. Brennan *et al.* analyzed the linear-FMCW radar signal detailedly and presented an innovative processing scheme, including data rotation, zero-padding phase normalization of the range-processed radar signal for convenient calculation of the precise range, along with the timing synchronization consideration. However, the common phenomenon named frequency ramp nonlinearity is not paid much attention in Paul's research.

The existence of frequency ramp nonlinearity could severely limit the performance of range profile via increased range sidelobes [6], [12]. The high range sidelobes of strong signals may mask weaker internal layers, arising ambiguities in interpreting data [13], [17]. The frequency ramp nonlinearity can be characterized as random and periodic deviations [9]. The random subpart is caused by the phase noise, which also has influence on signal-to-noise ratio (SNR) [9], [22]. The periodic deviations are mainly caused by the frequency nonlinearity of the chirp generator and undesired spurious signals generated from the nonlinear group delay of the filters in the radar system [5], [9]. After the received signal mixed with the instantaneous transmitted signal, the transmitted nonlinearity is overlapped with the received nonlinearity in the beat frequency signal, thus the nonlinearity problem depends on the round-trip delay time [12]. In addition, the distortions of the transmitting and receiving antennas also have effects on the overlapped nonlinearity [13].

Manuscript received March 11, 2020; accepted June 18, 2020. Date of publication June 23, 2020; date of current version July 5, 2020. This work was supported in part by the National Natural Science Foundation of China under Grant 41606219 and Grant 41776186, in part by the Scientific Research Project of Beijing Educational Committee (KM 201910005027), and in part by the Rixin Fund of Beijing University of Technology. *(Corresponding author: Xiangbin Cui.)*

Shinan Lang, Yukai Zhao, Ben Xu, Yiheng Cai, and Qiang Wu are with the Faculty of Information Technology, Beijing University of Technology, Beijing 100124, China (e-mail: langshinan@gmail.com; 649471834@qq.com; 877266460@qq.com; caiyiheng@bjut.edu.cn; wuqiang@bjut.edu.cn).

Xiangbin Cui is with the Polar Research Institute of China, Shanghai 200136, China (e-mail: cuixiangbin@pric.org.cn).

Xiaojun Liu is with the Key Laboratory of Electromagnetic Radiation and Sensing Technology and the Institute of Electronics, Chinese Academy of Sciences, Beijing 100190, China (e-mail: lxjdr@mail.ie.ac.cn).

Digital Object Identifier 10.1109/JSTARS.2020.3004357

Both hardware and software solutions have been proposed to solve the frequency ramp nonlinearity problem [13]. Since the hardware approaches are either too expensive or too complex [12], a lot of effects have thus been dedicated to the development of software methods. Li *et al.* [13], Yan *et al.* [5], [6], and Panzer *et al.* [7] suggested to add system response deconvolution to their ordinary range processing scheme, which is similar to Paul's method, to remove the nonlinearity. The kernel of the additional deconvolution is the proper estimation of the system transfer function, which contains the overlapped nonlinearity. The improper estimations would potentially raise the noise floor and reduce SNR [5], [6]. The state-of-the-art estimation method is using a standard adaptive filter, such as the least mean square (LMS) filter to compare the actual recorded beat frequency signal and a synthetic sinusoid [5], [6]. The actual recorded beat frequency signal used here could be obtained either through a combination of the outcomes of radar system-loopback measurement and antenna measurement in the microwave anechoic chamber [13] in the case of surface-based measurement, or approximated by the return over natural or man-made calibration targets, such as a corner reflector [5], [6], during airborne field deployment. Once the system transfer function is determined, its inverse can be convolved with the collected radar data to achieve the nonlinearity elimination. The current estimated system transfer function does not give sufficient thought to the effect of round-trip time dependence, that is, the recorded radar data involved with the IRHs at different depths would be deconvolved with the system transfer function estimated at a fixed distance. The fixed distance is determined by the length of selected delay line or the survey altitude of the aircraft. In addition, the LMS filter is sensitive to noise level [27]. Hence, the precision of the nonlinearity elimination will decrease to some extent.

In this article, we initially analyze the nonlinear signal model of the surface-based FMCW ice-sounding radar. On the basis of the established nonlinear signal model, a novel range processing method is proposed to accomplish the high-precision range profile via adding an innovative nonlinearity elimination strategy into the ordinary range processing scheme. The innovative nonlinearity elimination strategy handles the transmitted nonlinearity integrated with the impact of antennas' distortions and the received nonlinearity separately to cope with the impact of round-trip time dependence. The strategy first accomplishes the transmitted nonlinearity estimation via performing the proposed root homomorphic deconvolution scheme [18] integrated with the unwrapping method on the measurement result of a delay line. The proposed deconvolution scheme could deal with the phase ambiguity and has robustness to the existence of noise. Subsequently, the fractional system transfer function merely containing the transmitted nonlinearity integrated with the impact of antennas' distortions is achieved by combing the transmitted nonlinearity estimation result and the measurement result for transmitting and receiving antennas in the microwave anechoic chamber. At this point, the 1-D inverse filtering named the acceleration Richardson–Lucy (R–L) deconvolution algorithm [20], [21] is implemented to counteract the transmitted nonlinearity and the impact of antennas' distortions in consideration of alleviating the ill-posed problem and promoting the noise robustness. Finally, the residual video phase (RVP) removal technique [19] is applied to eliminate the dependence of nonlinearity on round-trip delay time to simplify the received nonlinearity elimination. Compared with the aforementioned nonlinearity removal method, our proposed nonlinearity elimination strategy takes full consideration of the dependence of nonlinearity on the round-trip delay time while providing certain robustness of noise.

The rest of this article is organized as follows. In Section II, we analyze the nonlinear signal model. The theoretical analysis and applied procedures of the proposed range processing method are outlined in Section III. In Section IV, we validate our algorithm by simulating different kinds of frequency ramp nonlinearities with different SNRs. We compare the imaging results of ice sheets obtained from our algorithm with those from Li's algorithm [13]. We discuss and conclude our work in Section V.

II. Nonlinear Signal Model of the Surface-Based FMCW Ice-Sounding Radar

The transmitted chirp signal of the FMCW ice-sounding radar bearing nonlinearity phase modulation could be modeled as follows:

$$s_t(t) = \exp\left[j2\pi\left(f_{\min}t + \frac{K}{2}t^2 + e(t)\right)\right] \tag{1}$$

where $f_{\min}$ denotes the start frequency of the sweep, t denotes the fast time, K denotes the frequency sweep rate, and $e(t) = P_p(t) + P_n(t)$ denotes the nonlinearity phase modulation. The periodic nonlinearity $P_p(t)$ could be approximated by developing it into an infinite Taylor series, and characterized as a summation of sinusoid functions with different weights [9]. Hence, the periodic nonlinearity can be mainly divided into polynomial nonlinearity and sinusoidal nonlinearity. Moreover, $P_n(t)$ is the random frequency ramp nonlinearity.

Ignoring the motion under the narrow-beamwidth approximation and ice surface slope-induced phase shift [1], the received signal of surface-based FMCW ice-sounding radar is an attenuated and delayed copy of transmitted signal, which is given by

$$s_r(t,\tau) = \exp\left\{j2\pi\left[f_{\min}(t-\tau) + \frac{K}{2}(t-\tau)^2 + e(t-\tau) + P_{\mathrm{at}}(t)\right]\right\} \tag{2}$$

where τ denotes the round-trip delay time for the wave propagation, and $P_{\mathrm{at}}(t)$ denotes the phase deviation caused by the antenna distortions, whose frequency response $P_{\mathrm{at}}(f)$ could be measured in the microwave anechoic chamber.

After the deramping operation, the beat frequency signal, i.e., the intermediate frequency (IF) signal, can be expressed as

$$\begin{aligned} s_{\mathrm{IF}}(t,\tau) =\ & \exp\left[j2\pi\left(f_{\min}\tau + Kt\tau\right) - j\pi K\tau^2\right. \\ & \left. + j2\pi\left(e(t) - e\left(t-\tau\right)\right) - j2\pi P_{\mathrm{at}}(t)\right] \\ =\ & s_{\mathrm{IF\_ideal}}(t,\tau)s_{\mathrm{RVP}}(\tau)s_d(t,\tau) \end{aligned} \tag{3}$$

where $s_{\mathrm{IF\_ideal}}(t,\tau) = \exp[j2\pi(f_{\min}\tau + Kt\tau)]$ is the undisturbed IF signal expected to be retrieved, $s_{\mathrm{RVP}}(\tau) = \exp(-j\pi K\tau^2)$ is the RVP term, and $s_d(t,\tau)$ is the overlapped

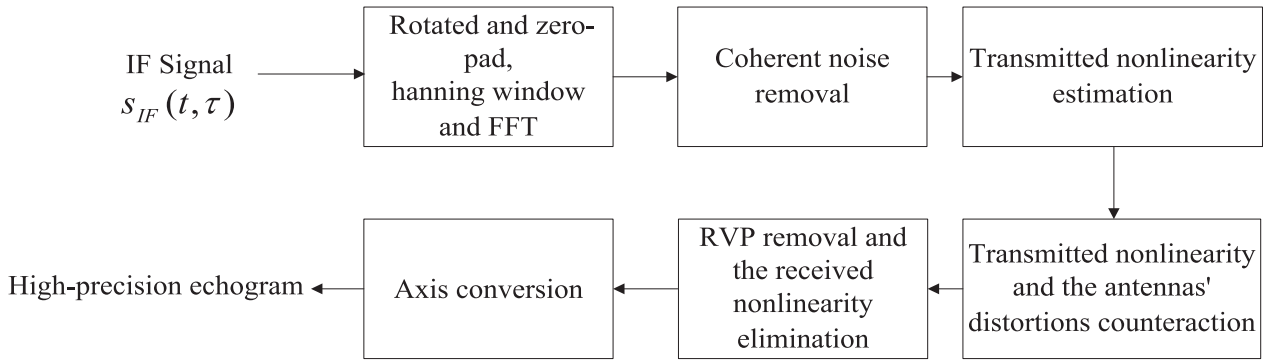

Fig. 1. Flowchart of the proposed range processing method.

disturbance signal, which is obviously depends on the round-trip delay time τ, i.e.,

$$s_d(t,\tau) = \exp\left[j2\pi\left(e(t) - e\left(t-\tau\right)\right)\right] \cdot \exp\left(-j2\pi P_{\mathrm{at}}(t)\right) \tag{4}$$

where $\exp[j2\pi(e(t) - e(t-\tau))]$ is the overlapped nonlinearity, and $\exp(-j2\pi P_{\mathrm{at}}(t))$ is the impact of antennas' distortions.

III. Proposed Signal Processing Strategy

A. Overview

The proposed range processing method is designed to obtain the high-precision range profile via adding innovative nonlinearity removing scheme into the ordinary range processing schemes. The processing steps are shown in Fig. 1, which includes the following.

1) The IF signal $s_{\mathrm{IF}}(t,\tau)$ given in (3) is rotated and zero-pad, followed by a fast Fourier transform (FFT) to obtain a preliminary frequency-intensity echogram $s_{\mathrm{IF}}(f,\tau)$. Here, a Hanning window is applied to preliminarily reduce the sidelobe levels at a small expense of the range resolution [5].
2) Coherent noise removal is applied by subtracting the slow-time mean from the data.
3) The proposed root homomorphic deconvolution scheme integrated with the unwrapping method is applied to the measurement result of a delay line to obtain the transmitted nonlinearity estimation $e(f)$ in frequency domain. The fractional system transfer function containing the transmitted nonlinearity integrated with the impact of antennas' distortions is achieved by combing $e(f)$ and $P_{\mathrm{at}}(f)$.
4) The acceleration R–L deconvolution algorithm is implemented to counteract the transmitted nonlinearity and the impact of antennas' distortions.
5) The RVP removal technique is applied to eliminate the dependence of nonlinearity on τ and remove the RVP term $s_{\mathrm{RVP}}(\tau)$. The acceleration R–L deconvolution algorithm is performed once again to eliminate the received nonlinearity consistently, and thereby obtaining the undisturbed IF signal.
6) To accomplish the final unambiguously high-precision echogram, the beat-frequency axis of the undisturbed IF signal should be converted into a range axis. The range offset adjustment is implemented to guarantee the accuracy of the axis conversion.

B. Transmitted Nonlinearity Estimation

The overlapped nonlinearity $s_e(t,\tau)$ could be considered as the difference of the transmitted nonlinearity and its attenuated and delayed copy. Hence, the transmitted nonlinearity must be estimated at first. Due to the overlapped nonlinearity could be assessed with the controllable delay line technology without changing its amplitude easily, the problem is turned into estimating the original signal from the overlapped signal with definite time delay, which is quite similar with the multipath interference in communication signal processing. This kind of problem is generally resolved via the homomorphic deconvolution strategy [16]. In 2013, Yang *et al*. have involved the homomorphic deconvolution algorithm to complete the nonlinearity correction of FMCW SAR [12]. Their strategy could easily deal with the dependence of round-trip delay time τ, whereas two inherent shortcomings of the homomorphic deconvolution are not taken into consideration [16]: the poor robustness of various noise and the phase ambiguity. To overcome these two disadvantages, the root homomorphic deconvolution scheme integrated with the unwrapping method is proposed in this article to achieve the transmitted nonlinearity estimation of the surface-based FMCW ice-sounding radar. Thereinto the root homomorphic deconvolution scheme is adopted to deal with the phase noise, and the unwrapping method is used to eliminate the phase ambiguity.

The overlapped nonlinearity in the IF signal provided by loopback measurement using a delay line can be expressed as a convolution model [12], [16], which is given as

$$\Phi(t,\tau_{\mathrm{ref}}) = e(t) \otimes p(t,\tau_{\mathrm{ref}}) \tag{5}$$

where $\Phi(t, \tau_{\mathrm{ref}})$ denotes the overlapped nonlinearity provided by loopback measurement, τ_{ref} denotes the delay time provided by the delay line, and $p(t,\tau_{\mathrm{ref}}) = \delta(t) - \delta(t-\tau_{\mathrm{ref}})$ denotes an impulse function series. The robustness of the deconvolution does not suffer from the length of τ_{ref}, which has been verified in [12]. Thus, the chosen of τ_{ref} is easy to be implemented in practice via off-the-shelf controllable delay line device in laboratory. The FFT is implemented to obtain the spectrum of

$\Phi(t, \tau_{\mathrm{ref}})$ as

$$\Phi(\omega, \tau_{\mathrm{ref}}) = e(\omega) \cdot [1 - \exp(-j\pi\tau_{\mathrm{ref}})] \tag{6}$$

where ω is the center angular frequency. Thereafter, the *w*-plane phase unwrapping technique [24] is applied to (6), in order to eliminate the phase ambiguity. The operation procedures of *w*-plane phase unwrapping are given as follows. $\Phi(\omega, \tau_{\mathrm{ref}})$ is first transformed into a phase plane, which is the so-called *w*-plane. Then, each of the obtained instant phases is compared with three kinds of distinct phase characters. Finally, the unwrapped instant phase is achieved by a branch-cut processing. Performing the root compressed spectral density operation $|\cdot|^{\gamma}$ [25] on the (6) after phase unwrapping process, the output is given as

$$|\Phi(\omega, \tau_{\mathrm{ref}})|^{\gamma} = |e(\omega)|^{\gamma} + |1 - \exp(-j\pi\tau_{\mathrm{ref}})|^{\gamma} \tag{7}$$

where $-1 < \gamma < 1$ indicates the root parameter. The logarithmic operation used in the traditional homomorphic deconvolution is instead by $|\cdot|^{\gamma}$ operation for solving the noise amplification problem.

$|1 - \exp(-j\pi\tau_{\mathrm{ref}})|^{\gamma}$ term in (7) can be expanded as a Taylor series as follows:

$$|1 - \exp(-j\pi\tau_{\mathrm{ref}})|^{\gamma} = -\sum_{k=1}^{\infty} \frac{\prod_{1}^{k}(\gamma - k + 1)}{k!} \exp(-j\pi k\tau_{\mathrm{ref}}) \tag{8}$$

where *k* is the number of dividing range time *t* of $\Phi(t, \tau_{\mathrm{ref}})$ by τ_{ref}.

Substitute (8) into (7) and perform IFFT, the overlapped frequency ramp nonlinearity in the root cepstrum domain is given by

$$\hat{\Phi}(t, \tau_{\mathrm{ref}}) = \hat{e}(t) - \sum_{k=1}^{\infty} \frac{\prod_{1}^{k}(\gamma - k + 1)}{2\pi k!} \delta(t - k\tau_{\mathrm{ref}}) \tag{9}$$

where the symbol $\hat{}$ in (9) denotes the signal in the root cepstrum domain.

In order to obtain the transmitted nonlinearity, a comb notch filter is designed to eliminate the δ-series in (9). The generated comb notch filter is a filter with an amplitude of 0 at the points $t = k\tau_{\mathrm{ref}}$ and $\mathrm{value}_{\mathrm{SNR}}$ at other points, where $\mathrm{value}_{\mathrm{SNR}}$ is the estimated SNR of the received signal. The time width of the filter is the same as $\Phi(t, \tau_{\mathrm{ref}})$, and the number of notches is $k - 1$. After the root cepstrum filtering, $\hat{e}(t)$ is reverted from the overlapped nonlinearity. Now, the FFT, followed by the $|\cdot|^{1/\gamma}$ operation, is performed on $\hat{e}(t)$ to obtain the estimated transmitted nonlinearity $e(f)$ in frequency domain. Combined with $P_{\mathrm{at}}(f)$ determined in the microwave anechoic chamber by measuring the impulse responses of the antennas [26], the fractional system transfer function is achieved.

C. Nonlinearity Elimination

1) Removal of Transmitted Nonlinearity and Antennas' distortions: Considering the inherent ill-posed problem of inverse filtering [16] and the existing phase noise caused deviation $P_n(t)$ among $e(t)$, the acceleration R–L deconvolution algorithm is implemented to complete the 1-D inverse filtering to counteract the transmitted nonlinearity and the impact of antennas' distortions.

The acceleration R–L deconvolution algorithm attempts to maximize the likelihood of $s_{\mathrm{IF}}(f, \tau)$ by using the expectation–maximization algorithm. This algorithm has been proven to obtain accuracy reconstruction result when the noise level is high, due to it is derived from a different noise realization [21]. Thus, the elimination of transmitted nonlinearity and antennas' distortions is an iteration procedure as follows:

$$s_{\mathrm{IF\_re}}^{m+1}(f, \tau) = s_{\mathrm{IF\_re}}^{m}(f, \tau) \left(h^{*}(f) \frac{s_{\mathrm{IF}}(f, \tau)}{h(f) \otimes s_{\mathrm{IF\_re}}^{m}(f, \tau)} \right) \tag{10}$$

where $s_{\mathrm{IF\_re}}(f, \tau)$ indicates the IF signal only containing RVP term and received nonlinearity, $h(f)$ indicates the fractional system transfer function acquired in aforementioned section, $\otimes$ denotes the convolution operation, and *m* is the iteration index. For the purpose of speeding up the algorithm to convergence faster, the acceleration method based on vector extrapolation [20] is used. The acceleration method could adjust the iteration step length and path flexibly. The acceleration parameter chose in our algorithm uses higher-order terms in the Taylor series of $s_{\mathrm{IF\_re}}(f, \tau)$ to predict more than one step ahead, which could promote the accuracy of the prediction process and the effective during latter iterations when the reconstruction is changing very slowly.

2) RVP Removal and Received Nonlinearity Elimination: At present, the RVP removal technique [19] is applied to both eliminate the dependence of received nonlinearity on τ and remove the RVP term $s_{\mathrm{RVP}}(\tau)$. Afterward, the acceleration R–L deconvolution algorithm is performed once again to eliminate the received nonlinearity consistently, i.e.,

$$s_{\mathrm{IF\_ideal}}^{m+1}(f, \tau) = s_{\mathrm{IF\_ideal}}^{m}(f, \tau) \left(\varepsilon^{*}(f) \frac{s_{\mathrm{IF\_re\_RVP}}(f, \tau)}{\varepsilon(f) \otimes s_{\mathrm{IF\_ideal}}^{m}(f, \tau)} \right) \tag{11}$$

where $s_{\mathrm{IF\_re\_RVP}}(f, \tau)$ indicates the IF signal only containing received nonlinearity, and $s_{\mathrm{IF\_ideal}}(f, \tau)$ indicates the retrieved undisturbed IF signal in frequency domain.

D. Range Axis Construct

To take the advantage of the fine range conversion derived from the phase of $s_{\mathrm{IF\_ideal}}(f, \tau)$, the range offset adjustment should be implemented [22]. First, a reference function multiply is performed on $s_{\mathrm{IF\_ideal}}(f, \tau)$ to complete the zero-phase transfer to the center of each range bin and cancel the time delay caused by missynchronization [22]. The reference function is $ref = \exp[-j2\pi(f_{\min}\tau + K\Delta t\tau)]$, where Δt denotes the effect of a known timing error. Then Vernierlike process [22] is used to combine the coarse result with the fine result of range conversion to construct the final range axis. The coarse result indicates range of a given target to the nearest range bin, which is given by

$$R_{\mathrm{coarse}} = \frac{c}{2B\sqrt{\varepsilon_r}} \cdot \frac{n}{p} \tag{12}$$

where *c* is the speed of light, ε_r is the typical dielectric constant of snow or firn ice, *B* is the chirp bandwidth, *n* is the number

TABLE I
SIMULATION PARAMETERS WITH AN IDEAL TARGET

Parameter Name	Value	Units
Radar Style	FMCW	---
Target distance	40	m
Operating frequency	0.5-2	GHz
Sweep time	4	ms
PRF	6.25	kHz
Delay time τ_{ref}	492	ns
Antenna	Vivaldi	---

of the nearest range bin, and p is the pad factor introduced by zero-pad operation in Step 1). The fine result is calculated using the phase of same range bin, i.e.,

$$R_{\text{fine}} = \frac{cT}{2B\sqrt{\varepsilon_r}} \cdot f_b \tag{13}$$

where T is duration of the chirp, and f_b is the beat frequency.

IV. RESULTS AND COMPARISONS

A. Simulation

We conduct simulations to demonstrate the validity of the proposed range processing method. In order to make a comprehensive performance evaluation, the simulations have the following contents.

1) The accuracy of transmitted nonlinearity estimation is appraised.
2) The ability of nonlinearity elimination is evaluated by selecting several typical periodic nonlinearities $P_p(t)$ under the assumption that the phase noise keeps constant throughout the elimination simulations.
3) The robustness of noise during nonlinearity elimination is assessed via adjusting the value of $P_n(t)$ along with the fixed periodic nonlinearity.

In the simulation, an ideal target is setup at 40 m away from the radar system in free space. The undisturbed IF signal and the RVP term demonstrated in (3) are simulated using the parameters given in Table I. The frequency response $P_{\text{at}}(f)$ is consistent with the measurement result for antenna array equipped in our ultrawideband FMCW ice-sounding radar system, which will be discussed in Section IV-B specifically. The delay time τ_{ref} is set in accordance with our controllable delay line device of the shelf [29].

First, the accuracy of transmitted nonlinearity estimation is appraised. The appraisement is divided into two parts: the varying $P_p(t)$ with fixed $P_n(t)$, and the varying $P_n(t)$ with fixed $P_p(t)$. For the first situation, the quadratic, cubic, and sinusoid periodic nonlinearities are taken into consideration to give a full-scale simulation [9], [12]. The SNR is fixed via setting $P_n(t)$ to form the value of 20 dB. Fig. 2(a), (c), and (e) shows the performances of the transmitted nonlinearity estimation, respectively. Moreover, the estimation biases of each model are in the same order and less than 0.15, which are demonstrated in Fig. 2(b), (d), and (f), to make a more clear representation. Both the performances and the biases in Fig. 2 indicate that the proposed range processing method could provide convincing performances of transmitted nonlinearity estimation for varying kinds of periodic nonlinearity models. For the second situation, $P_p(t)$ is set as quadratic nonlinearity, whereas the SNR is adjusted via modulating $P_n(t)$ to form the values of 30 and 10 dB. Fig. 3(a) and (c) shows the performances of the transmitted nonlinearity estimation, respectively. In addition, the estimation biases of each SNR are illustrated in Fig. 3(b) and (d). Both of the biases are in the same order and less than 0.15. The results in Fig. 3 indicate that the proposed range processing method could indeed afford certain robustness of noise during transmitted nonlinearity estimation.

Afterward, the ability of frequency ramp nonlinearity elimination is evaluated under the assumption that the phase noise keeps constant throughout the elimination simulations. The estimated nonlinearities in Fig. 2(a), (c), and (e) are taken into consideration to give a full-scale simulation. The range responses of the final undisturbed IF signal are illustrated in Fig. 4(a)–(c) denoted by red-solid curves, respectively. To check on the elimination in more detail, the range responses only after processing Steps 1) and 2) are also shown in Fig. 4(a)–(c) denoted by blue-dashed curves, respectively. The peak sidelobe ratios (PSLRs) of the red curves are –19.75, –20.07, and –21.47 dB, respectively, whereas the blue curves are –9.214, –7.859, and –11.71 dB, respectively. The reductions of PSLRs are 10.536, 12.481, and 9.76 dB, respectively, which mean the frequency ramp nonlinearity has indeed been corrected in noise condition along with the appearances of red curves are basically symmetrical. The simulations also indicate that the proposed range processing method has almost the same capability of nonlinearity elimination while dealing with different kinds of nonlinearities in noise conditions.

Finally, the robustness of noise during nonlinearity elimination is assessed via adjusting the value of $P_n(t)$ along with the fixed periodic nonlinearity. The estimated nonlinearities in Fig. 3(a) and (c) are adopted to achieve the assessment. The range responses of the final undisturbed IF signal with different SNRs are denoted by the red-solid curves in Fig. 5(a) and (b), respectively. The corresponding results merely after processing Steps 1) and 2) are also given for comparisons, denoted by the blue-solid curves in Fig. 5(a) and (b), respectively. The PSLRs of the red curves are –31.92 and –19.19 dB, respectively, whereas the blue curves are –9.85 and –7.448 dB, respectively. The reductions of PSLRs are 22.07 and 11.742 dB, respectively, which indicate that the frequency ramp nonlinearity has been eliminated in varying noise conditions along with the appearances of red curves are basically symmetrical.

B. Field Deployment Results

This section illustrates the accuracy of the proposed range processing method of imaging of IRHs using real firn ice data. The real firn ice data are collected by our designed ultrawideband FMCW ice-sounding radar named shallow-layers-detection ice-sounding radar (SLDISR). The key SLDISR parameters are given in Table II. The measured return loss of the antenna array is shown in Fig. 6, and the normalized patterns of each frequency point between 0.5 to 2 GHz are given in [28]. Since the 29th Chinese Antarctic Research Expedition (CHINARE

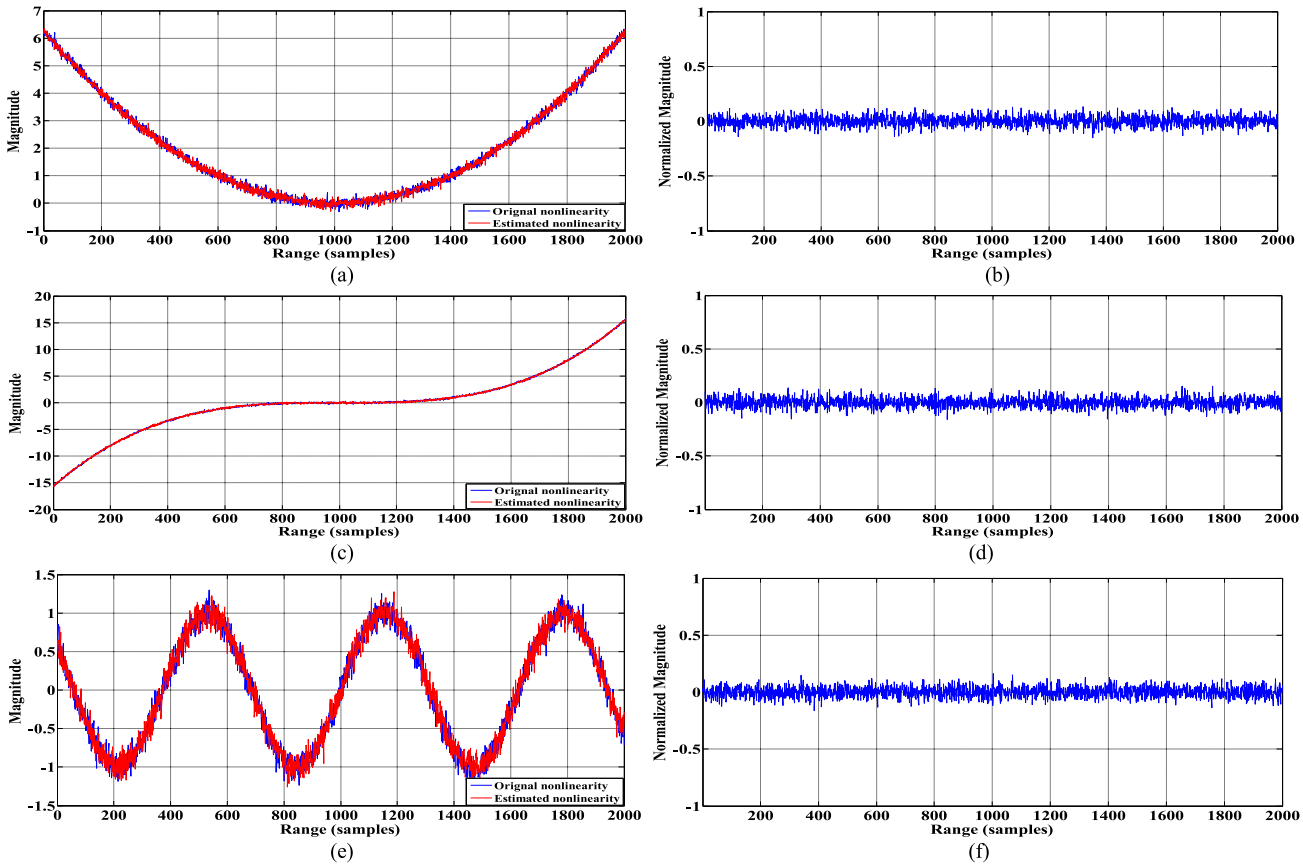

Fig. 2. Evaluation of transmitted nonlinearity estimation accuracy—Situation 1: varying $P_p(t)$ with fixed $P_n(t)$. (a) Quadratic nonlinearity simulation. (b) Estimation bias of quadratic nonlinearity. (c) Cubic nonlinearity simulation. (d) Estimation bias of cubic nonlinearity. (e) Sinusoid nonlinearity simulation. (f) Estimation bias of sinusoid nonlinearity.

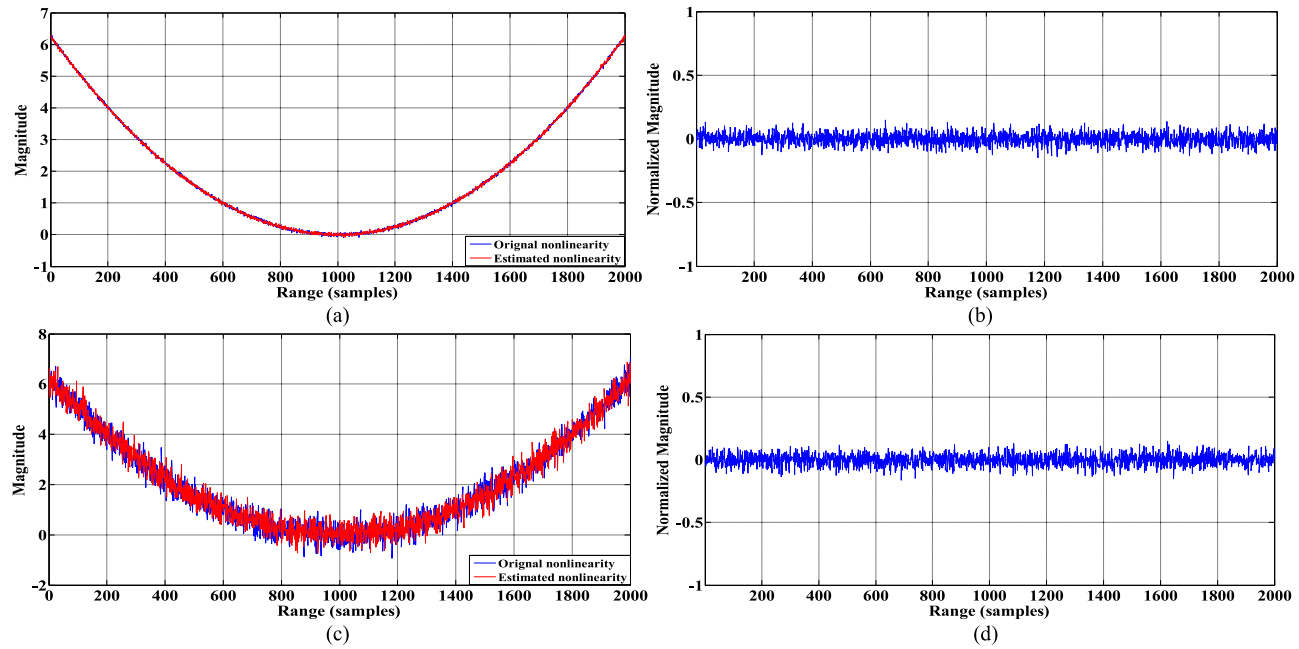

Fig. 3. Evaluation of transmitted nonlinearity estimation accuracy—Situation 2: varying $P_n(t)$ with fixed $P_p(t)$. (a) SNR $=$ 30 dB. (b) Estimation bias of SNR $=$ 30 dB. (c) SNR $=$ 10 dB. (d) Estimation bias of SNR $=$ 10 dB.

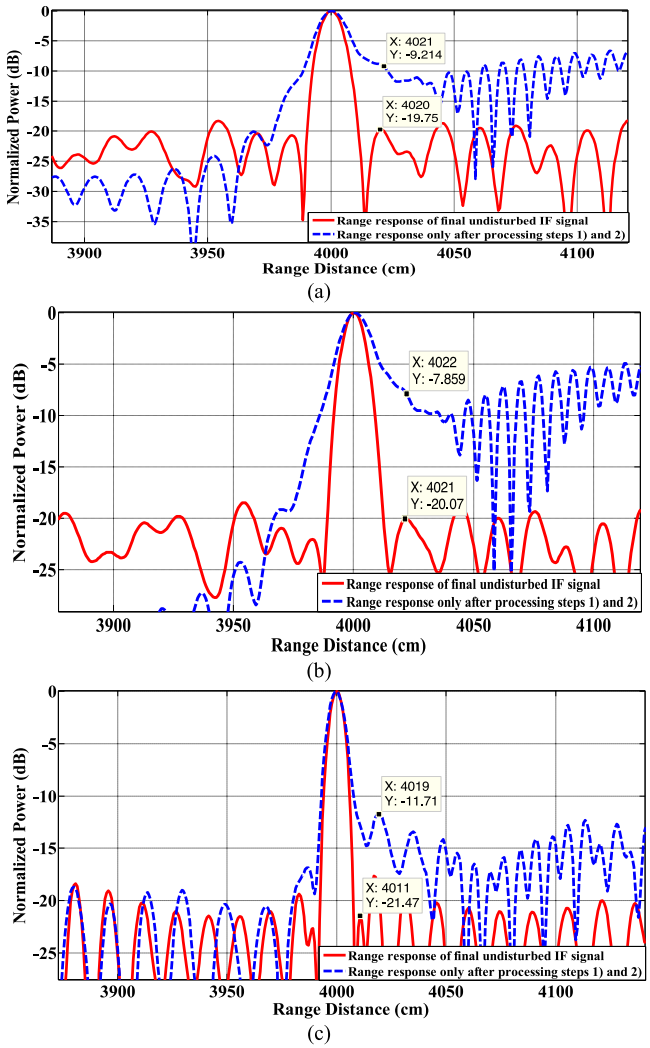

Fig. 4. Range responses for evaluation of the frequency ramp nonlinearity elimination ability: consistent noise situation. (a) Range response with quadratic nonlinearity simulation. (b) Range response with cubic nonlinearity simulation. (c) Range response with sinusoid nonlinearity simulation.

TABLE II
BASIC SLDISR RADAR PARAMETERS

Parameter Name	Value	Units
Radar Style	FMCW	---
Oscillator	YIG	---
Operating altitude	2	m
Operating frequency	0.5-2	GHz
Theoretical resolution (firn-ice)	6.61	cm
Sweep time	4	ms
PRF (Initial)	200	kHz
PRF (After coherent integration)	6.25	kHz
Transmit power	500	mW
ADC	1.47-GSPS 16-b	---
Antenna	Vivaldi	---

29), the SLDISR has been deployed over East Antarctic Ice Sheet for measurements of IRHs and snow/firn accumulation over land ice for four times. We select two samples of SLDISR data corresponding to CHINARE 31 and 33 in this section. Our controllable delay line device [29] has the fixed delay length of 492 ns in free space. The waveform of measured $\Phi(t, \tau_{\mathrm{ref}})$ is

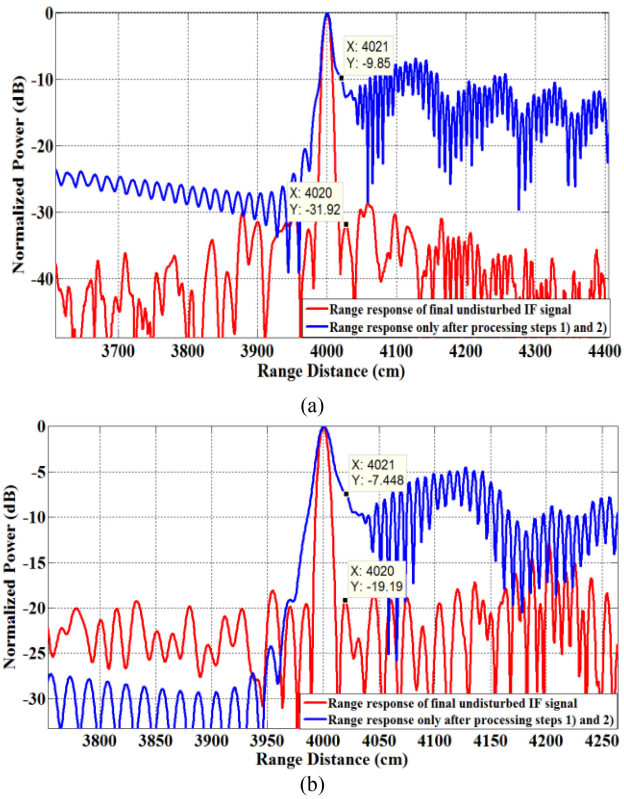

Fig. 5. Range responses for assessment of robustness of noise during nonlinearity elimination: fixed periodic nonlinearity. (a) Range response with SNR of 30-dB simulation. (b) Range response with SNR of 10-dB simulation.

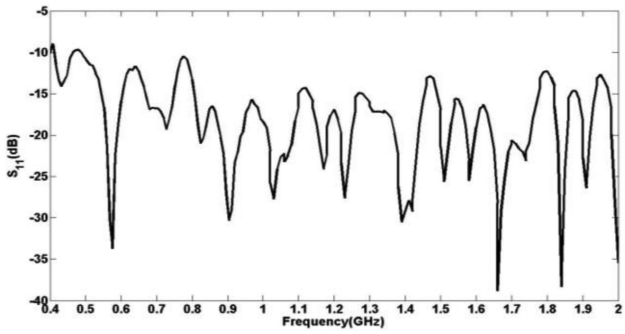

Fig. 6. Measured return loss of the array.

shown in Fig. 7. The sounder-derived profiles after the proposed range processing strategy are shown in Figs. 8(a) and 9(a). The A-scopes corresponding to the black-dashed lines in Figs. 8(a) and 9(a) are displayed in Fig. 10(a) and (b), indicated by red curves.

In order to demonstrate the advantages of the proposed processing method, the echograms obtained by Li's algorithm [13] are illustrated in Figs. 8(b) and 9(b), whereas the A-scopes corresponding to the black-dashed lines are shown by the blue curves in Fig. 10(a) and (b). Since our SLDISR is designed merely for surface-based condition, the system transfer function is estimated by using LMS filter to compare the actual recorded beat frequency signal and a synthetic sinusoid. The

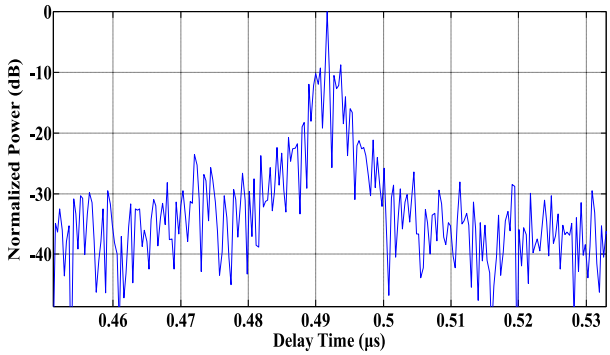

Fig. 7. Waveform of measured $\Phi(t, \tau_{\mathrm{ref}})$ via our controllable delay line device.

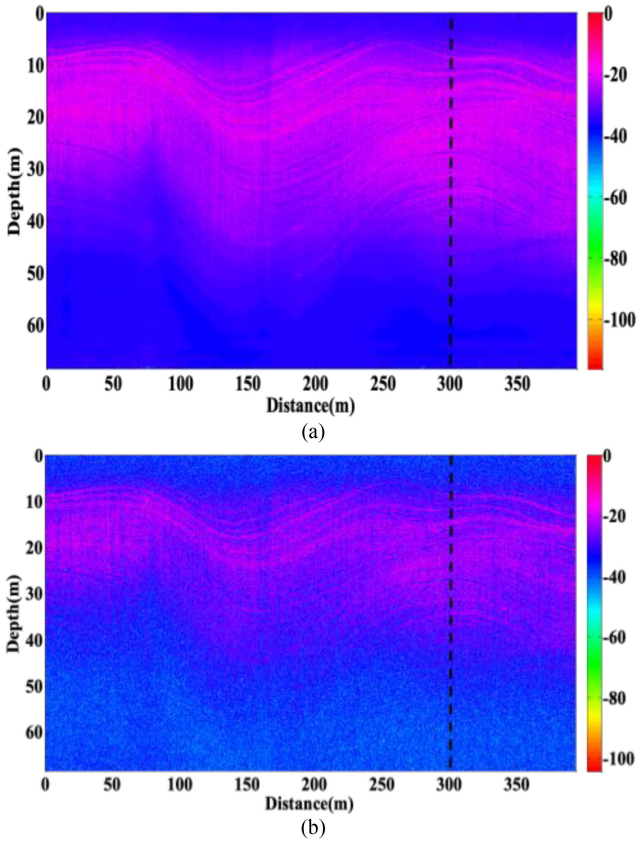

Fig. 8. Results of SLDISR data collected during CHINARE 31 (data number: 113202). (a) Proposed range processing strategy result. (b) Result of Li's algorithm [13]. The vertical stripes in both echograms between 50 to 100 m and 150 to 200 m in the along-track direction are caused by the difference in instantaneous phases [30]. The detected layers fade out at a very shallow depth, which makes it seem likely that full coherent link budget of radar system has not been achieved.

actual recorded beat frequency signal is obtained through a combination of $\Phi(t, \tau_{\mathrm{ref}})$ and antenna array measurement.

On the one hand, we compared the results of our algorithm with others in near sidelobe suppression via A-scope comparisons. The enlarged A-scopes in Fig. 10(a) demonstrate the comparison of distinct layer approached to depth 18 m. The difference between the mainlobe and near sidelobe of the red curve is 10.783 dB, whereas this difference of the blue curve

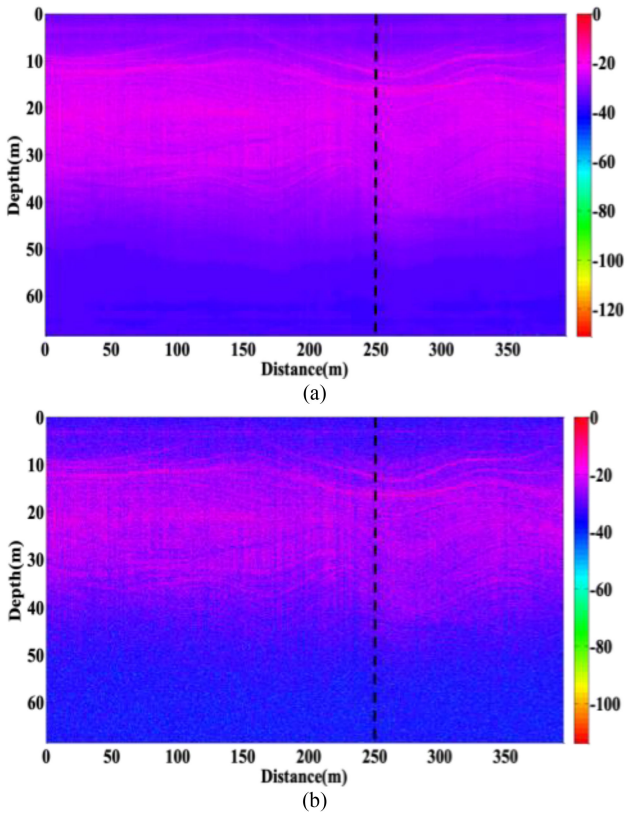

Fig. 9. Results of SLDISR data collected during CHINARE 33 (data number: 143943). (a) Proposed range processing method result. (b) Result of Li's algorithm. The vertical stripes in both echograms in the along-track direction are caused by the difference in instantaneous phases as well.

is 2.33 dB. Meanwhile, the mainlobe width of the red curve is narrower than the blue curve. The enlarged A-scopes in Fig. 10(b) illustrate the distinct layer approached to depth 20 m. The difference between the mainlobe and near sidelobe of red curve is 10.844 dB, whereas this difference of the blue curve is 9.184 dB. Moreover, the mainlobe width of the red curve is narrower than the blue curve as well. The higher suppression of near sidelobe and narrower mainlobe width in comparisons indicate that our range processing method has a better ability in range sidelobes suppression.

On the other hand, we compared the echograms of our algorithm with others via estimated SNR of the echogram. The estimated SNR is calculated by [16] as follows:

$$\mathrm{SNR}_{\mathrm{est}} = 10 \lg \left(\frac{{\sigma_l}^2 (i,j)}{{\sigma_\xi}^2 (i,j)} \right) \tag{14}$$

where ${\sigma_l}^2(i,j)$ denotes the local variance, and ${\sigma_\xi}^2(i,j)$ denotes the noise variance. ${\sigma_l}^2(i,j)$ and ${\sigma_\xi}^2(i,j)$ are calculated by (15) via selecting different kinds of areas in the same echogram [16]

$$\sigma^2 (i,j) = \frac{1}{(2M+1)(2Q+1)} \times \sum_{k=-M}^{M} \sum_{l=-Q}^{Q} \left[\boldsymbol{D}(i+k, j+l) - \mu (i,j) \right]^2 \tag{15}$$

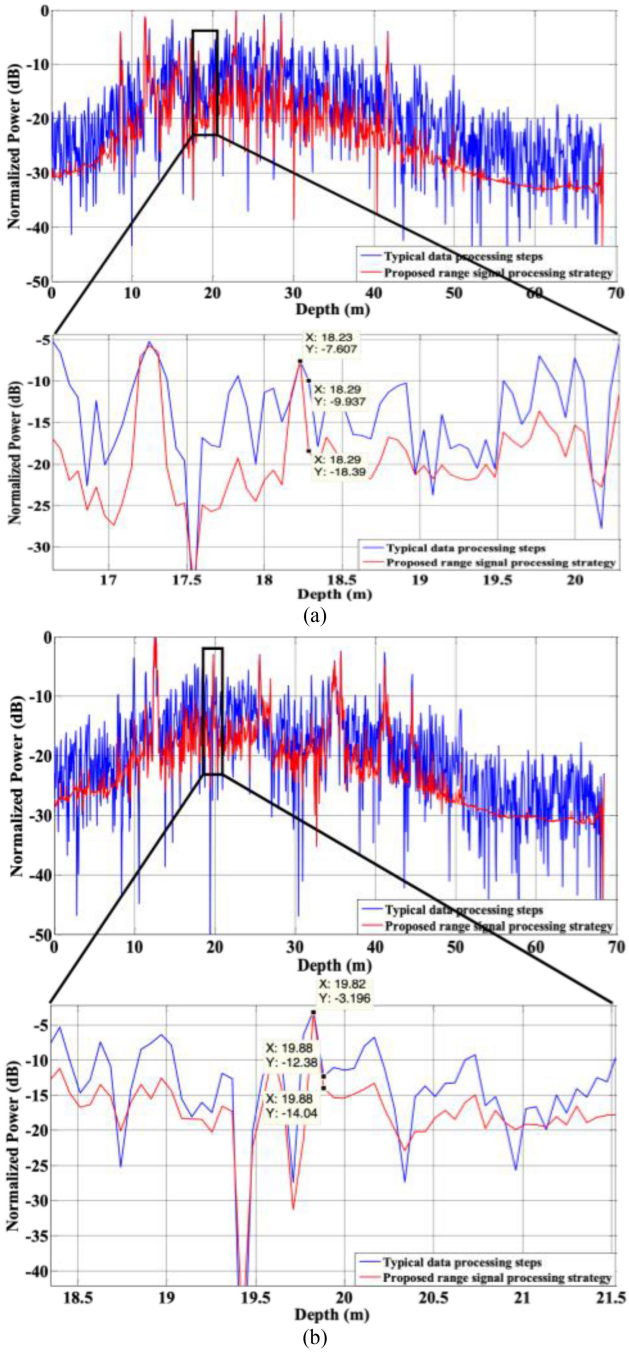

Fig. 10. Comparisons between A-scopes. (a) A-scopes corresponding to the black-dashed lines of Fig. 8(a) and (b). (b) A-scopes corresponding to the black-dashed lines of Fig. 9(a) and (b). The red curves denote the proposed algorithm, and the blue curves denote the typical data processing steps.

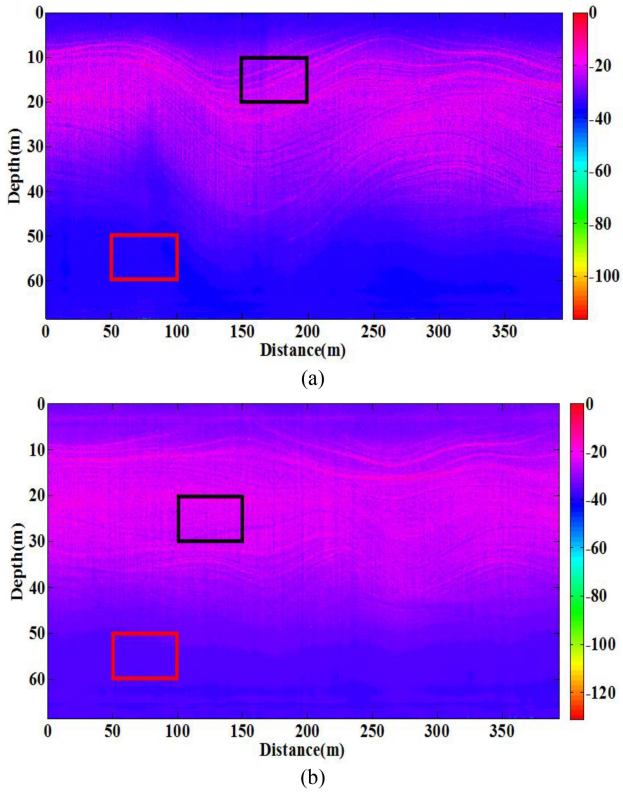

Fig. 11. Areas for calculating SNR. (a) Areas for calculating SNR of Fig. 8(a) and (b). (b) Areas for calculating SNR of Fig. 9(a) and (b). The black squares denote the area for calculating local variance, and the red squares denote the area for calculating noise variance.

where (i, j) is the pixel location; M and Q is the size of calculation window whose values often select $M = Q = 2$ (window size 5×5), and $\boldsymbol{D}$ is the calculation area. According to the selecting rule defined in [16], we choose the area (10 m, 20 m)×(150 m, 200 m) of Fig. 8(a) and (b) and the area (20 m, 30 m)×(100 m, 150 m) of Fig. 9(a) and (b) to calculate ${\sigma_l}^2(i, j)$, which are demonstrated by black squares in Fig. 11(a) and (b). Analogously, the areas (50 m, 60 m) × (50 m, 100 m) of Figs. 8 and 9(a) and (b) are elected to calculate ${\sigma_\xi}^2(i, j)$, which are demonstrated by red squares in Fig. 11(a) and (b). $\mu(i, j)$ denotes the local mean calculated by

$$\mu\,(i,j) = \frac{1}{(2M+1)(2Q+1)} \sum_{k=-M}^{M} \sum_{l=-Q}^{Q} \boldsymbol{D}(i+k, j+l). \tag{16}$$

From (14) to (16), the estimated SNRs of Fig. 8(a) and (b) are 38.8890 and 13.2010 dB, respectively, whereas the values of Fig. 9(a) and (b) are 33.3914 and 13.4740 dB, respectively. The comparisons of estimated SNR show that the proposed range processing strategy has stronger ability in range sidelobes suppression and noise elimination than typical range processing scheme.

Through the preceding comparisons, we can conclude that our range processing method removes the nonlinearity effectively in the case of unknown kinds of periodic nonlinearities and phase noises within the real data. Furthermore, its property in nonlinearity elimination is superior to the typical range processing scheme.

V. Discussion and Conclusion

In this article, we have established the nonlinear signal model of the surface-based FMCW ice-sounding radar, and demonstrated a novel range processing method, which aims at

effectively removing the frequency ramp nonlinearity. In the simulations, we validate the proposed algorithm's capability of estimating and eliminating the nonlinearity by using several typical periodic nonlinearities and varying phase noises. The comparisons done with SLDISR data indicate that the proposed range processing method removes the nonlinearity better.

The proposed processing method could be easily applied to the airborne circumstance with proper revision of the measurement of system transfer function (see Section I). Our algorithm will be applied to the large dataset acquired during CHINARE 29, CHINARE 31, and CHINARE 33 to improve data interpretation and the analysis of the snow/firn accumulation. Meanwhile, we are currently developing an automated layer tracking algorithm that searches for the IRHs correctly based upon a combination of snake algorithm and the curvelet transform.

Acknowledgment

The authors would like to thank CHINARE 29, CHINARE 31, and CHINARE 33, and the teammates for their generous help in the experiments in Antarctica. The authors would like to thank Prof. B. Sun and Prof. J. Guo of the Polar Research Institute of China, and Prof. Y. Dou, Y. Pan, and Dr. G. Zuo of the Taiyuan University of Technology for their valuable assistance in data acquisition over Antarctica. The authors would also like to thank D. Li from the Key Laboratory of Electromagnetic Radiation and Sensing Technology of Chinese Academy of Sciences, for developing the SLDISR system.

References

[1] J. Paden, "Synthetic aperture radar for imaging the basal conditions of the polar ice sheets," Ph.D. dissertation, Dept. Elect. Eng. Comput. Sci., Univ. Kansas, Lawrence, KS, USA, 2006.

[2] M. E. Peters, D. D. Blankenship, S. P. Carter, S. D. Kempf, D. A. Young, and J. W. Holt, "Along-track focusing of airborne radar sounding data from West Antarctica for improving basal reflection analysis and layer detection," *IEEE Trans. Geosci. Remote Sens.*, vol. 45, no. 9, pp. 2725–2736, Sep. 2007.

[3] X. Liu *et al.*, "High-resolution ice-sounding radar measurements of ice thickness over east antarctic ice sheet as a part of Chinese national Antarctic research expedition," *IEEE Trans. Geosci. Remote Sens.*, vol. 56, no. 7, pp. 3657–3666, Jul. 2018.

[4] R. Wang, O. Loffeld, H. Nies, S. Knedlik, M. Hägelen, and H. Essen, "Focus FMCW SAR data using the wavenumber domain algorithm," *IEEE Trans. Geosci. Remote Sens.*, vol. 48, no. 4, pp. 2109–2118, Apr. 2010.

[5] J. Yan *et al.*, "Airborne measurements of snow thickness: Using ultrawideband frequency-modulated-continuous-wave radar," *IEEE Geosci. Remote Sens. Mag.*, vol. 5, no. 2, pp. 57–76, Jun. 2017.

[6] J. Yan *et al.*, "Ultrawideband FMCW radar for airborne measurements of snow over sea ice and land," *IEEE Trans. Geosci. Remote Sens.*, vol. 55, no. 2, pp. 834–843, Feb. 2017.

[7] B. Panzer *et al.*, "An ultra-wideband, microwave radar for measuring snow thickness on sea ice and mapping near-surface internal layers in polar firn," *J. Glaciol.*, vol. 59, no. 214, pp. 244–254, 2013.

[8] J. A. Uribe, R. Zamora, G. Gacitúa, A. Rivera, and D. Ulloa, "A low power consumption radar system for measuring ice thickness and snow/firn accumulation in Antarctica," *Ann. Glaciol.*, vol. 55, no. 67, pp. 39–48, 2014.

[9] S. Ayhan, S. Scherr, A. Bhutani, B. Fischbach, M. Pauli, and T. Zwick, "Impact of frequency ramp nonlinearity, phase noise, and SNR on FMCW radar accuracy," *IEEE Trans. Microw. Theory Techn.*, vol. 64, no. 10, pp. 3290–3301, Oct. 2016.

[10] N. Galin *et al.*, "2–8 GHz FMCW radar for estimating snow depth on Antarctic Sea ice," in *Proc. IEEE Radar Conf.*, Rome, Italy, May 26–29, 2008, pp. 276–281.

[11] F. Ulaby, R. Moore, and A. Fung, *Microwave Remote Sensing Volume II: Radar Remote Sensing and Surface Scattering and Emission Theory*. Reading, MA, USA: Addison-Wesley, 1982, p. 120.

[12] J. Yang, C. Liu, and Y. Wang, "Nonlinearity correction of FMCW SAR based on homomorphic deconvolution," *IEEE Geosci. Remote Lett.*, vol. 10, no. 5, pp. 991–995, Sep. 2013.

[13] J. Li *et al.*, "Deconvolution of FMCW radars for operation IceBridge missions," in *Proc. United States Nat. Committee URSI Nat. Radio Sci. Meeting*, Boulder, CO, USA, Jan. 8–11, 2014, p. 1.

[14] D. Gomez-Garcia, F. Rodriguez-Morales, C. Leuschen, and S. Gogineni, "Ku-band radar altimeter for surface elevation measurements in polar regions using a wideband chirp generator with improved linearity," in *Proc. IEEE Geosci. Remote Sens. Symp.*, Munich, Germany, 2002, pp. 4617–4620.

[15] J. B. Yan, S. Gogineni, D. Braaten, J. Brozena, F. Rodriguez-Morales, and E. Arnold, "Ultra-wideband radars operating over the frequency range of 2-18 GHz for measurements on terrestrial snow and ice," in *Proc. IEEE Geosci. Remote Sens. Symp.*, Beijing, China, 2016, pp. 7078–7081.

[16] Z. Mouyan, *Deconvolution and Signal Recovery*, vol. 4. Beijing, China: Nat. Defence Ind. Press, 2001, pp. 97–101.

[17] R. Kwok and C. Haas, "Effects of radar side-lobes on snow depth retrievals from operation IceBridge," *J. Glaciol.*, vol. 61, no. 227, pp. 576–584, 2015.

[18] P. Alexandre, J. Boudy, and P. Lockwood, "Root homomorphic deconvolution schemes for speech processing in car noise environments," in *Proc. IEEE Int. Conf. Acoust., Speech, Signal Process.*, Minneapolis, MN, USA, Apr. 27–30, 1993, pp. 99–102.

[19] A. Meta, P. Hoogeboom, and L. P. Ligthart, "Signal processing for FMCW SAR," *IEEE Trans. Geosci. Remote Sens.*, vol. 45, no. 11, pp. 3519–3532, Nov. 2007.

[20] D. S. C. Biggs and M. Andrews, "Acceleration of iterative image restoration algorithms," *Appl. Opt.*, vol. 36, no. 8, pp. 1766–1775, Mar. 1997.

[21] J. Svensson, "High resolution frequency estimation in an FMCW radar application," M.S. dissertation, Dept. Elect. Eng., Linköping Univ., Linköping, Sweden, 2018.

[22] P. V. Brennan, L. B. Lok, K. Nicholls, and H. Corr, "Phase-sensitive FMCW radar system for high-precision Antarctic ice shelf profile monitoring," *IET Radar Sonar Navig.*, vol. 8, no. 7, pp. 776–786, Aug. 2014.

[23] I. G. Cumming and F. H. Wong, *Digital Processing of Synthetic Aperture Radar Data*, vol. 3. Boston, MA, USA: Artech House, 2005, p. 92.

[24] S. T. Kaplan, "Phase unwrapping: A review of methods and a novel technique," in *Proc. CSPG CSEG Conv.*, 2007, pp. 534–537.

[25] T. Kobayashi and S. Imai, "Spectral analysis using generalised cepstrum," *IEEE Trans. Acoust., Speech, Signal Process.*, vol. 32, no. 6, pp. 1235–1238, Dec. 1984.

[26] F. Zhang, Y. Ji, and G. Fang, "A compact Vivaldi antenna for 0.5-2 GHz," *J. Microw.*, vol. 26, no. 6, pp. 54–57, Dec. 2010.

[27] Z. Xianda, *Modern Signal Processing*, vol. 4, 2nd ed. Beijing, China: Tsinghua Univ. Press, 2002, pp. 188–192.

[28] F. Zhang, "Research on optimized designing methods and application techniques of wideband antennas," Ph.D. dissertation, Dept. Electromagn. Field Microw. Technol., Graduate School Chin. Acad. Sci., Beijing, China, 2011.

[29] 2019. [Online]. Available: http://www.cofiber.net/product/showproduct.php?id=277

[30] D. Castelletti, D. M. Schroeder, E. Mantelli, and A. Hilger, "Layer optimized SAR processing and slope estimation in radar sounder data," *J. Glaciol.*, vol. 65, no. 254, pp. 983–988, Oct. 2019.

Shinan Lang (Member, IEEE) received the B.E. degree from the University of Science and Technology Beijing, Beijing, China, in 2010, the M. S. and Ph.D. degrees in electromagnetic field and microwave technology from the Institute of Electronics, Chinese Academy of Sciences, Beijing, China, in 2013 and 2015, respectively.

Since 2015, she has been a Lecturer with the Faculty of Information Technology, School of Information and Communications Engineering, Beijing University of Technology, Beijing, China. Her research interests include developing advanced signal and array processing algorithms for processing and interpreting data of radio echo sounding of ice sheets, and radar depth sounder image processing technology.

Xiangbin Cui received the Ph.D. degree in geological resources and geological engineering from the Department of Earth Sciences, Zhejiang University, Hangzhou, China, in 2010.

After Ph.D., he joined the Polar Research Institute of China, Shanghai, China, and focuses on studying the Antarctic ice sheet and its potential change through both grounded and airborne ice penetrating radar survey. He became Associate Professor in 2016. He has been to Antarctica for four times, and has good experience in geophysical survey design and operation in Antarctica.

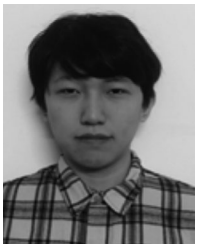

Yukai Zhao received the B.E. degree and the M.S. degree in computer technology from the Beijing University of Technology, Beijing, China, in 2017 and 2020, respectively.

He has been to Antarctica during CHINARE 35 to complete the radio echo sounding data processing. His research interest includes high-performance computing for processing data of radio echo sounding of ice sheets.

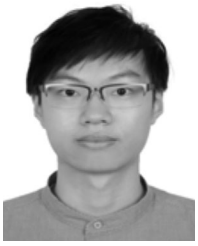

Ben Xu received the B.E. degree, in 2019 from the Beijing University of Technology, Beijing, China, where he is currently working toward the M.S. degree in information and communication engineering with the Faculty of Information Technology, School of Information and Communications Engineering.

His research interest includes developing signal processing algorithms for processing and interpreting data of radio echo sounding of ice sheets.

Xiaojun Liu received the B.S. and M.S. degrees in electronics science and technology from the North University of China, Taiyuan, China, in 1995 and 1998, respectively, and the Ph.D. degree in electrical engineering from the Chinese Academy of Sciences (CAS), Beijing, China, in 2001.

Since 2001, he has been with the Key Laboratory of Electromagnetic Radiation and Sensing Technology, CAS, where he is currently a Professor and leads a group on the researches of remote sensing of ice sheets with projects supported by the National Natural Science Foundation of China, National High Technology Research and Development Projects (863 Projects) of China, etc. He developed several radar systems currently being used at the Institute of Electronics, CAS, for sounding and imaging of polar ice sheets. These radar systems have been used in field experiments in Antarctica for five times since CHINARE 26. In the field of lunar and deep space exploration, he leads a group to demonstrate the scheme of subsurface penetrating radar of Mars orbiter and vehicle for China's first Mars exploration. The program has been adopted and is being implemented. His research interests include application of radars to the remote sensing of the polar ice sheets, ionosphere, and land.

Yiheng Cai (Member, IEEE) received the Ph.D. degree in pattern recognition and intelligent system from the Beijing University of Technology, Beijing, China, in 2006.

She is currently an Associate Professor with the Faculty of Information Technology, Beijing University of Technology. She has authored or coauthored more than 60 papers in journals, books, and conferences. Her research interests include image processing and pattern recognition.

Prof. Cai is the member of the China Computer Federation.

Qiang Wu received the B.S. and M.S. degrees from the North University of China, Taiyuan, China, in 1995 and 1998, respectively, and the Ph.D. degree from the Beijing University of Technology, Beijing, China, in 2011.

From 1998 to 2006, he was a Lecturer and from 2006 to 2016, an Associate Professor with the College of Electronic Information and Control Engineering, Beijing University of Technology. Since 2016, he has been a Professor with the School of Information and Communications Engineering, Beijing University of Technology. He currently leads a group on the researches of embedded system with projects supported by the National Natural Science Foundation of China, National High Technology Research and Development Projects (863 Projects) of China, etc. His research interests include high performance, high-speed real-time system, multimedia information processing, DSP, and embedded systems.